Nanoscale

PAPER

View Article Online
View Journal | View Issue

Cite this: *Nanoscale*, 2020, **12**, 3692

Zn doped $MAPbBr_3$ single crystal with advanced structural and optical stability achieved by strain compensation†

Ruxue Li,‡[a,b] Shaoqing Chen,‡[c] Xia Li,‡[c,d] Guoxin Yin,[c] Youpin Gong,[a,e] Jiahao Yu,[a] Guotao Pang,[a] Jianxun Liu,[a] Yanjun Liu,[a] Zhenhua Ni,[b] Liyuan Zhang,[e] Rui Chen *[a] and Hsing-Lin Wang*[c]

A mechanistic understanding of perovskite degradation is one of the most urgent issues to push perovskite devices toward commercial applications. Surface coverings will lower the electrical injection and light extraction efficiency of perovskites. Therefore, structural modification of Zn doped perovskites has been proposed herein. The Zn doping will induce local lattice strain due to smaller ionic radius. It is interesting that the lattice structure at atomic resolution has been observed directly through cryo-TEM. Under light illumination, the photostriction will compensate for the local lattice strain, which leads to structural stability as evidence suggests no phase transition in temperature ranges of the temperature-dependent photoluminescence spectra. In addition, MPZB also shows less than 3% decrease in PL intensity after 60 days. This is because the Zn doping induced the lowest defect density in the MPZB SC (density of trap-states n_{trp} = 6.33 × 10^8 cm^{-3}), which has been confirmed by the high performance of the photodetector. Such strain compensation is expected to fundamentally improve the stability of photoelectric devices.

Received 12th November 2019,
Accepted 2nd January 2020

DOI: 10.1039/c9nr09657d

rsc.li/nanoscale

Introduction

Halide perovskites have a three-dimensional structural framework of ABX_3, where A is a monovalent organic cation (*e.g.*, methylammonium ($CH_3NH_3^+$, namely MA^+), formamidinium ($CH(NH_2)^{2+}$, namely FA^{2+}) or inorganic cation (Cs^+, Rb^+, K^+), B is a metal cation (*e.g.*, Pb/Mn/Sn/Ge/Cu/Sb/Bi/Cd/Zn), and X is a halide anion (I^-, Br^-, Cl^-). Its structure can be viewed as a cubic array of corner-sharing [BX_6] octahedra with A located within the cages or a cubic close-packed [AX_3] array with B located within the holes.[1–3] Though halide perovskites have been known for more than 60 years, they have recently attracted intensive research interest after their initial application in photovoltaics, reported by Kojima *et al.* in 2009,[4] and now single-junction organic–inorganic hybrid halide perovskite solar cells have recorded an efficiency of 24.02%.[5] This value is comparable to those of conventional photovoltaics such as crystalline silicon, CdTe, GaAs, and CuInGaSe based devices.[2] Beyond their application in photovoltaics,[6] halide perovskites possess advanced optoelectronic properties, such as a high absorption coefficient in the visible region,[1] long balanced hole–electron diffusion length,[7] high carrier mobility,[7] and long carrier lifetime,[8,9] which make them good candidates for light-emitting diodes (LEDs),[10] lasers[11] and photodetectors[10] *etc.*

However, there are still several serious problems that restrict the development of perovskite devices, including the presence of harmful Pb^{2+} ions and their poor stability in moisture, high temperature and intensive light illumination.[12,13] Many strategies have been proposed to improve the environmental stability of perovskite materials, such as encapsulating perovskites with organic or inorganic materials,[14] adding porous silicon microspheres for better dispersion,[15] adding a hydrophobic material to increase hydrophobicity[16] and through passivation to reduce the non-radiative recombination centers of the material[17] *etc.* However, the surface coating of perovskites with thick shells will restrict their efficiency in terms of electrical injection and light extraction. In addition, for any given perovskite, the structural phase transition has been commonly observed at different temperatures, which greatly influenced the performance of optoelectronic

[a]*Department of Electrical and Electronic Engineering, Southern University of Science and Technology, Shenzhen, Guangdong 518055, P. R. China.*
E-mail: chenr@sustech.edu.cn
[b]*School of Physics, Southeast University, Nanjing, Jiangsu 211189, P. R. China*
[c]*Department of Materials Science and Engineering, Southern University of Science and Technology, Shenzhen, Guangdong 518055, P. R. China.*
E-mail: wangxl3@sustech.edu.cn
[d]*State Key Laboratory of Inorganic Synthesis and Preparation Chemistry, College of Chemistry, Jilin University, Changchun, 130012, P. R. China*
[e]*Department of Physics, Southern University of Science and Technology, Shenzhen, Guangdong 518055, P. R. China*

†Electronic supplementary information (ESI) available. See DOI: 10.1039/c9nr09657d

‡These authors contributed equally to this work.

devices.[18,19] Therefore, it is essential to improve the stability of perovskite materials through structural modification.

The substitution of cations or halide anions is an effective method to change the structure of perovskites and this has recently attracted widespread attention.[20,21] For example, the most well-known organic cations to replace the MA^+ ion are the FA^+ or Cs^+ ions, which give rise to a tolerance factor (t) of 0.88 ($MA_{1-x}FA_xPbI_3$) and 0.9 ($FA_{1-x}Cs_xPbI_3$), both higher than 0.83 for $MAPbI_3$.[18,22] The tolerance factor t is used to determine the stability of the perovskite structure. It is more likely to form a cubic structure if t is in the range of 0.89–1.0, while smaller t values give less-symmetric tetragonal or orthorhombic structures.[18,19] It should be noted that the black cubic-phase $CsPbI_3$ is not stable at room temperature.[23] Moreover, the substitution of halide anions may remarkably affect the band gap, crystal structure and charge transport of the perovskite, due to its unique energy band structure caused by halide anions.[15] Therefore, the substitution of Pb^{2+} cation is one of the most important and promising methods for improving perovskite stability. To find a non-toxic element to replace toxic Pb^+ for improved stability has been a common goal for researchers.[24] However, the formation energy of B-site cations is higher than those of the A-site cations and X-site halide ions,[3] which makes them more difficult to synthesize.[20] There are a wide variety of cations with different atomic radii that may induce huge changes in perovskites, and the structural stability of perovskites must consider the octahedral factor μ related to B site cations.[22] Also, the stability of the B-site doping is still an important issue of concern but lacks experimental support.[3,24] Therefore, the mechanistic understanding of how cation doping changes the photophysical properties and stability remains elusive. Research in this area is urgent and critical to the performance improvement of perovskites.

Zn is a non-toxic element which has a wide range of sources in nature. Its oxide is also an important material in the field of optoelectronics.[25] In this work, Zn has been incorporated into a MPB single crystal (SC). Through the studies of its structure, optical properties and photostability, it was found that Zn doping will cause shrinkage of the crystal lattice, resulting in enhanced coupling between atoms. Under light illumination, the photostriction leads to the relaxation of local lattice strain, and the sample shows improved emission in terms of temperature and time. Through analyzing the performance of the perovskite detector, it was found that the Zn doping is also beneficial to reduce the defect density in the SC, which is essential for advanced device performance. This work has provided a basis and reference for Zn doping in perovskite materials which will promote the development of perovskite applications.

Results and discussion

A hybrid perovskite SC was prepared by an inverse temperature crystallization method. For the $MAPbBr_3$ (MPB) sample, a solution containing 1 M $PbBr_2$ and MABr was prepared in 10 mL of DMF at room temperature. For the Zn-doped sample $MAPb_{1-x}Zn_xBr_3$ (MPZB), a solution containing 1 M MABr, 0.9 M $PbBr_2$ and 0.1 M $ZnBr_2$ was prepared in 10 mL of DMF at room temperature, as shown in Fig. 1a. The solutions were filtered using a PTFE filter with 0.2 mm pore size. Two milliliters of the filtrate were placed in a vial and kept in an oven at 80 °C for six months. The powder X-ray diffraction (XRD) patterns of the MPB and MPZB samples are shown in Fig. 1b. The measured diffraction peaks of the MPB SC in this work are in good agreement with previous reports,[8] which implies a pure cubic phase and the crystals of MPB and MPZB both belong to the cubic $pm\bar{3}m$ space group at room temperature. Moreover, the characteristic XRD peaks of all samples show narrow diffraction peaks indicating a higher degree of crystallinity. In addition, the Zn and Pb in the MPZB sample were obtained by inductively coupled plasma optical emission spectroscopy (ICP-OES), and the weight content ratio of Zn : Pb is 1.55 : 1000. To verify the successful Zn doping, transmission electron microscopy (TEM) characterization has been performed. It is important to note that the high resolution TEM (HRTEM) characterization of the SC cannot be measured with traditional TEM due to the

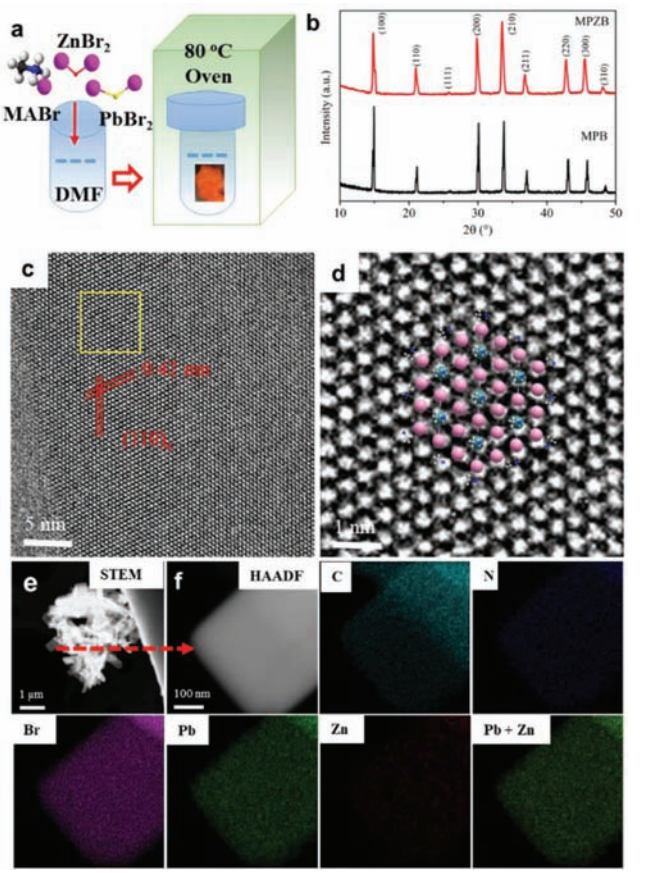

Fig. 1 Synthesis and structure of the MPZB SC. a. Schematic diagram of the growth of the MPZB sample. b. XRD patterns of the MPZB and MPB samples. c. High resolution TEM (HRTEM) image of the single crystal MPZB along the $[111]_c$ zone axis observed by cryo-TEM at liquid N_2 temperature. d. Magnified HRTEM image of the region in the yellow square of c image, overlapped with the corresponding atomic model. e and f. STEM image and STEM-EDS element mappings.

immediate damage of the material by the energetic electron beam. Herein, cryo-TEM was used to determine the structure of MPZB at the atomic scale. Fig. 1c shows the HRTEM image of the MPZB structure at the [111] zone. The lattice fringes with a d spacing of 4.2 Å corresponded to the $\{110\}_c$ planes, which agrees well with the XRD result. Fig. 1d shows the enlarged TEM image of the area in orange in Fig. 1c and clearly identifies the hexagonal lattice of MPZB, which corresponds to the $[111]_c$ projection of the structure model in the cubic structure. These results demonstrate that the structure of MPZB is still cubic at liquid nitrogen temperature. The energy dispersive spectrometer (EDS) mappings are shown in Fig. 1e and f, and imply that Zn atoms are homogeneously distributed within the MPB matrix. Green represents the content of Pb and red represents the content of Zn, both of which can be clearly identified.

The digital photographs of MPB and MPZB SCs are shown in Fig. 2a. An overview of partial cation exchange in the MPB SC is shown in Fig. 2b, where the $ZnBr_6$ octahedra are schematically depicted by the purple metal–halide octahedra, and the Pb cations are partially replaced by Zn cations by cation exchange reactions, resulting in divalent-cation-doped MPB NCs, namely the MPZB sample. Fig. 2c shows the PL and absorption spectra of the samples. The PL peak is slightly blue-shifted after Zn incorporation, which is in good agreement with the blue-shift observed in the UV-vis absorption spectrum. This blue-shift can be ascribed to the increase of the band gaps due to the increase of the interaction between B and X atoms and the decrease of the unit cell volume.[21] The Pb^{2+} and Zn^{2+} have different radii, electronic configurations and properties ($R_{Pb^{2+}}$ = 119 pm, electronegativity χ = 1.6; $R_{Zn^{2+}}$ = 74 pm, χ = 1.7). As Zn^{2+} has a significantly smaller radius than Pb^{2+}, the atomic lattice will suffer from a change in local strain.[21] According to the absorption spectra, emission at about 550 nm in MPB and 530 nm in MPZB can be ascribed to their energy band edge recombination, while the low energy shoulders come from the reabsorption of the crystal which has been observed in previous work.[26] It has been reported that the optical properties of perovskites can be modified by some means such as irradiation[27] and doping. While the band gaps of ABX_3 perovskites are known to increase with the decrease of the unit cell volume,[21] and the ionic radius of Zn is smaller than Pb, the observed blue-shift of the optical transitions is primarily due to the lattice contraction.

The optical stabilities in terms of the temperature of the samples have been characterized. As shown in Fig. 3a and b, pseudo-color maps of the temperature-dependent PL spectra of the samples have been plotted, while Fig. 3c shows the extracted PL peak position. This was recorded by using a Shamrock spectrometer and the samples were placed in a vacuum chamber under excitation by a 442 nm He–Cd continuous wave laser. Temperature can be well-controlled inside the closed-cycle helium cryostat between 40 and 300 K. It can be seen that there are two peaks (P_1 and P_2) that exist at different temperatures for both samples, and the P_1 emission shows a blue-shift while the P_2 shows a red-shift, which is consistent with the typical perovskite luminescence and reabsorption. Therefore, this implies that P_1 comes from the band edge emission, while P_2 comes from the reabsorption of the crystal. Furthermore, it is worth noting that there is a two-step red-shift (100–130 K and 200–220 K) for P_1 in the MPB sample, which implies the existence of structural phase transition across this temperature range, namely from orthorhombic to tetragonal and then to cubic. The structural phase transition temperatures are similar to previously reported values (150 and 240 K).[19] It is interesting to note that for peak P_1 in the MPZB sample, no obvious red-shift can be observed as shown in Fig. 3c, indicating the absence of structural phase transition for MPZB. This is important because advanced optoelectronic device application requires stable perovskite structures over the operating temperatures.[12] The temperature dependent integrated PL intensities of MPZB can be fitted using the Arrhenius equation:[28]

$$I(T) = \frac{I_0}{1 + A\exp\left(-\frac{E_b}{K_B T}\right)} \quad (1)$$

where I_0 is the PL intensity at 0 K, E_b is the activation energy, and K_B is the Boltzmann constant. The fitted data are shown

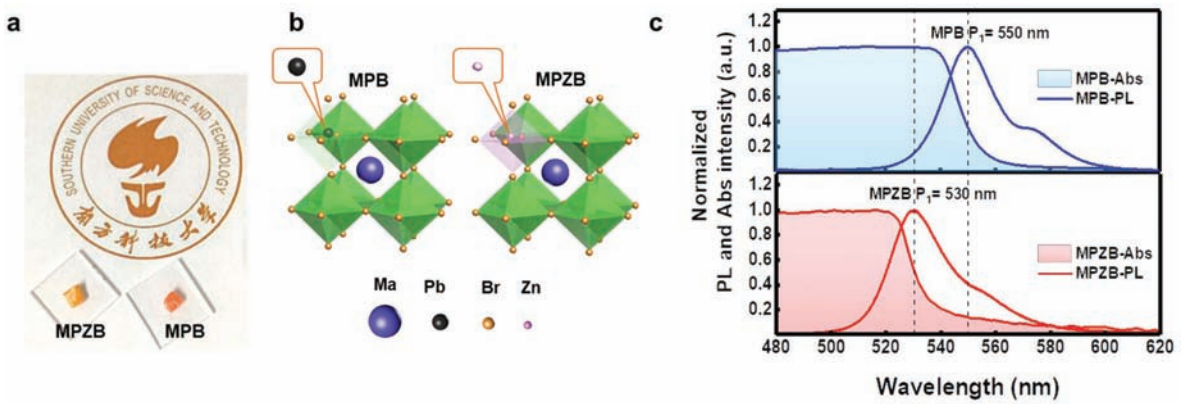

Fig. 2 Basic information of MPZB. a. Digital photographs of the MPB and MPZB samples. b. Schematic overview of partial cation exchange in perovskites. c. PL and absorption spectra of the MPB and MPZB samples.

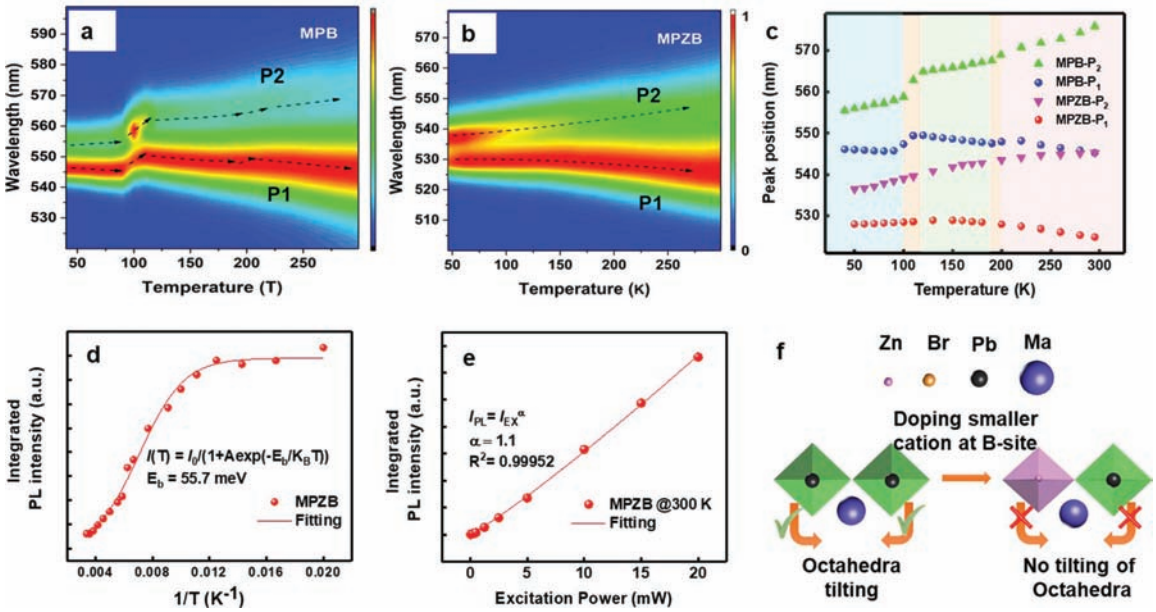

Fig. 3 Temperature-dependent PL of MPZB. a and b. Pseudo-color maps of temperature dependent PL spectra of the MPB and MPZB samples. c. PL peak position. d. Temperature dependence of the integrated PL intensity of the MPZB sample, and the solid line is the fitting line. e. Power dependent PL intensity. f. Schematic diagram of the octahedral tilting.

as solid lines in Fig. 3d. Based on the fitting, the activation energy E_b for MPZB was found to be 55 ± 3.5 meV, which was very close to the binding energy (40–50 meV) previously reported for MPB.[28] Note that this value is higher than the thermal energy at room temperature (26 meV) and exciton binding energy of GaN (25 meV), ensuring the existence of excitons at room temperature. This conclusion is also verified by the power dependent PL measurement (as shown in Fig. S1 and S2†). As shown in Fig. 3e, there is a power law dependence

$$I_{PL} = I_{EX}^{\alpha} \quad (2)$$

where α denotes the nonlinear component. The α value can be determined to be 1.1, confirming the excitonic characteristics of the spontaneous emission (note that $1 < \alpha < 2$ accounts for the recombination of free excitons and bound excitons).[28]

In contrast, for the MPB sample, eqn (1) is only valid for the temperature range where the perovskite material holds the same structural phase (as shown in Fig. S3†). This is why we need perovskite materials to be stable in the operating temperature range for device applications. It is reported that the optoelectronic properties of perovskites are very sensitive to their $[BX_6]^{4-}$ octahedral structures.[12,23] For example, just 12.5 mol% Mn-doping has the potential to reduce all (100%) of the cuboctahedral voids for metal ions in the perovskite lattice, whereas substitution with a smaller anion at the X-site can influence only four such cuboctahedral voids.[3] Thus, a minute amount of the Zn doping in perovskites may be an effective strategy to mitigate the aforesaid problems. During the optical measurement at different temperatures, many voids exist in the MPB sample inside the crystal. The bond energy is too weak to maintain the cubic structures, and then the $[BX_6]^{4-}$ octahedral structures will tilt when the lattice shrinks at lower temperatures and the voids become bigger. Moreover, the MPB sample possesses an anisotropic strained lattice, and intensive light illumination or higher temperatures might lead to the lattice cracking,[13] while for the MPZB sample, the Zn doping in the perovskite not only reduces the void inside the octahedron, but also enhances the interaction between octahedra, so that the octahedron retains the cubic structure when the temperature increases, as shown in Fig. 3f. In addition, the lattice strain due to Zn doping (the atomic radius of the Zn is smaller than Pb) will compensate the volume expansion under light illumination or higher temperatures, and thus it may lead to dramatically improved stability for the MPZB sample. To further address this hypothesis, photostability measurement was conducted and will be discussed next.

Normalized PL emission with temperatures and time is shown in Fig. 4, where the insets are the digital photographs of the samples under laser excitation at room temperature. It can be seen clearly from Fig. 4a that the PL intensity of the MPB sample decreases more than 2 orders of magnitude from 40 to 300 K, while that of the MPZB sample only reduces several times. This implies that the MPZB sample has less surface trapping or thermal activated nonradiative recombination centers compared to MPB.[25] Long-term photostability tests up to 60 days were performed under illumination by using a 325 nm continuous wave laser with power density around 70 mW cm^{-2}. Both samples were adhered to the quartz substrate and exposed to laser light directly at room temperature for 4 hours per day. As shown in Fig. 4b, the PL intensity

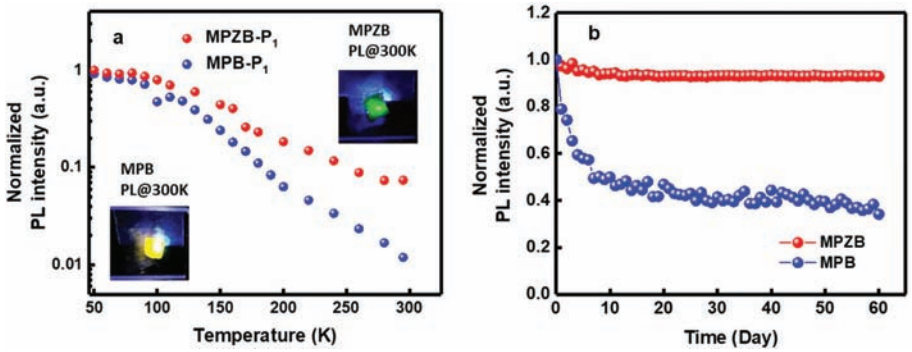

Fig. 4 Temperature stability and photostability of MPZB. a. Normalized PL intensity with temperatures. b. Measurements of long-term emission photostability.

of the MPB sample decreases to ~40% after 60 days, while the intensity of the MPZB sample remains almost the same. This can also be explained by the local lattice strain compensation. The MPZB suffers compressive strain due to the distorted lattice, which balances cations of different sizes. Upon illumination, it undergoes volumetric expansion in all directions. This process relaxes the local strain, reducing the defects (such as dislocation and grain boundary) of the crystallites and improving the lattice quality of the material and its stability.[23] This phenomenon is crucial for understanding the structural stability of perovskites, especially for perovskite optoelectronic device application.

The SC possesses a smaller number of grain boundaries, longer diffusion length and faster mobility than thin films. Therefore, it is a good candidate for photodetector devices.[8] Moreover, compared to conventional semiconductor materials, including polycrystalline Si (n_{traps} = 10^{13} to 10^{14} cm^{-3}),[29] CdTe/CdS (n_{traps} = 10^{11} to 10^{13} cm^{-3}),[30] and copper indium gallium selenide (CIGS) (n_{traps} = 10^{13} cm^{-3}) thin films,[31] as well as other perovskite materials, the defect density of the $MAPbX_3$ crystals was the lowest.[1,8] As discussed above, the Zn doping is indeed responsible for the improved structural stability. However, there is no report about the effect of Zn doping on the host's photoelectron properties. To this aim, a photodetector was fabricated based on the MPZB crystal as shown in Fig. 5a. The size of the MPZB SC photodetector is 2.67 × 2.35 = 6.275 mm^2 (digital photographs of the photodetector are shown in Fig. S4†), and ~50 nm thick Au electrodes were deposited *via* vacuum thermal evaporation. The current–voltage (*I*–*V*) characteristic of the MPZB sample was measured to evaluate its quality and photoelectric performance, as shown in Fig. 5b and c. In Fig. 5b, the dark current (J_D) of the device has three regions: an ohmic region, a trap-filled limit (V_{TFL}) region and a Child's region of the quadratic voltage dependence. Along with increasing bias voltage, the ohmic region

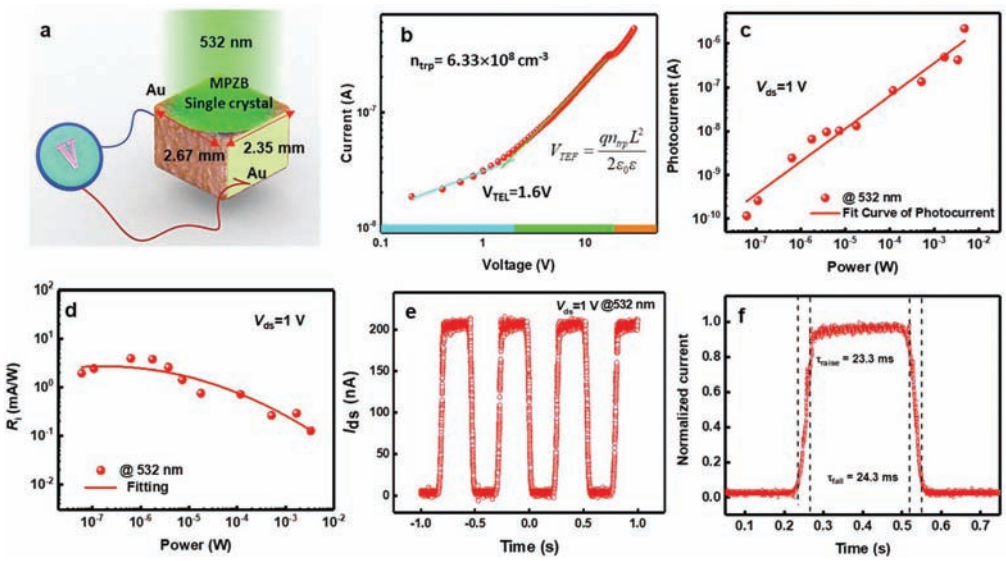

Fig. 5 Photodetection properties of MPZB. a. Schematic diagram of the MPZB photodetector. b. Dark current (J_D) of the device. c. The photocurrent increases with illuminated light intensity. d. Photoresponsivity (*R*) of the MPZB photodetector. e. Reproducible responses to light illumination. f. The response time of the photoconductor to light illumination.

followed by the V_{TFL} region, which is determined by the trap-state density (n_{trap}), can be used to estimate the density of the trap-states according to the formula,[9]

$$V_{TEF} = \frac{qn_{trp}L^2}{2\varepsilon_0\varepsilon} \quad (3)$$

where ε_0 is the dielectric constant of the material which is around 25,[8] ε_0 is the vacuum permittivity of 8.854×10^{-14} F cm^{-1}, q is the elemental charge, L is the thickness of the MPZB layer, and the V_{TEF} started at 1.6 V. From the equation, the density of trap-states $n_{trp} = 6.33 \times 10^8$ cm^{-3} can be extracted, which is significantly lower than those well-known perovskite SCs, as shown in Table 1 (in order to compare the accuracy, these detectors have similar structures). This is consistent with the high-resolution XRD measurement results that the as-prepared MPZB SCs exhibit high crystalline quality. In addition, the results also indicate the B-site Zn doping is responsible for reducing the defect density of MPB. This is beneficial to the improvement of the material's photoelectric properties by interdicting the process of light quenching, which is caused by absorbing impurities to increase radiative recombination centers. The photoresponse signal of the MPZB SC photodetectors is presented as a function of the input light intensity under the bias of 1 V as shown in Fig. 5c. The photoresponse of linear absorption generally increases linearly with the increase of luminescence. Fig. 5d shows the photo-responsivity (R) of the device under 1 V bias with 532 nm continuous laser illumination, and it decreases with the increased light intensity, which is in accordance with the photo-gating mechanism. The R is a crucial important figure-of-merit for photodetectors, indicating the efficiency of the response of a photodetector to an optical signal, and it is defined as the ratio of the photocurrent to incident light power,[32]

$$R = \frac{I_{ph}}{P_0 S} \quad (4)$$

where I_{ph} is the difference between the illuminated current and dark current:

$$I_{ph} = I_{illuminated} - I_{dark} \quad (5)$$

P_0 is the irradiance power density, and S is the effective illuminated area.

At low light intensity (≈600 nW), the $R \approx 3.9$ mA W^{-1} can be measured. Combining the value of the dark current and R, the detectivity D^* can be obtained according to

$$D^* = \frac{R\sqrt{A}}{\sqrt{qI_{dark}}} \quad (6)$$

The calculated D^* is about 2.36×10^{10} cm Hz$^{1/2}$ W^{-1} Jones (where A is the active area of the detector). To the best of our knowledge, these values are within the same order of magnitude among the recorded $MAPbX_3$ photodetectors with a similar structure, as shown in Tables 1 and 2.[7,33–40] Another crucial performance of the photodetectors is the response to light illumination, and it is required to be fast and reproducible enabling a broader scope of the device application. To illustrate the light-switching characteristic, the current under bright and dark conditions was controlled by using a shutter, and the devices promptly generated photocurrent with reproducible responses to on/off cycles. As shown in Fig. 5e, when the laser is turned on, the photocurrent is sharply increased under the applied 1 V bias voltage. The on/off switching was reproducible without any attenuation for multiple cycles, showing the favorable stability of the crystal-based detectors. The response time of the photodetectors to light illumination was analyzed and is shown in Fig. 5f. The rise and decay times (defined as the time necessary to reduce/increase the photoresponse from 90 to 10%) were determined to be 23.3 and 24.3 ms, respectively. This responding speed is faster than those found in similarly structured crystal photodetectors based on other hybrid perovskites, such as $MAPbCl_3$, $CsPbBr_3$ SC, as shown in Table 2. The faster photo-response of the MPZB SC photodetector could be attributed to the efficient charge transfer along the Zn to the $[BX_6]^{4-}$ octahedral structures, which results from the enhanced bond to bond interaction and the lower defect density. Once again, such strain compensation by the Zn doping under light illumination is not only responsible for the improved structural stability, but also for fewer defects, which is beneficial to the photoelectric properties of perovskites.

Table 1 Comparison of optical and electrical properties of perovskites

Sample	V_{TF} [V]	Dielectric constant (ε)	Trap density (n_{trap}) [cm^{-3}]	Carrier mobility (μ), [cm^2 V^{-1} s^{-1}]	Size [mm]	Year	Ref.
Au/Ti SC $MAPbCl_3$/Pt	9.8	23.9	3.1×10^{10}	42 ± 9	0.35	2015	33
Au/SC $MAPbaI_3$/Au & Au/SC $MAPbaI_3/C_{60}$/Ga	2.1–10.7	32	3.6×10^{10}	24.0 ± 6.8 (electron) 164 ± 25 (hole)	3	2015	7
ITO/SC $MAPbaI_3/MoO_3$/Au/Ag	24	—	3.3×10^{10}	2.5	$1.63 \times 2.74 \times 2.74$	2015	34
ITO/SC $MaPbaBr_3/MoO_3$/Au/Ag	4.6	25.5	5.8×10^9	38	—	2015	34
Ti/SC $CsPbBr_3$/Ti & Au/SC $CsPbBr_3$/Au	~7 (electrons) ~12 (holes)	22	1.1×10^{10} (electrons) 4.2×10^{10} (holes)	52 (electron) 11 (hole)	$3 \times 2 \times 1$	2017	36
ITO/Thin-Film $MAPbBr_3$/Au/Pt	—	—	1.6×10^{11}	60	380 nm	2018	37
Au/1D SC $MAPbBr_3$ Arrays/Au	1.7	—	1.9×10^{13}	—	10 μm	2018	38
planar gold interdigital electrodes/SC $MAPbBr_3$	12.4	25.5	5.2×10^9	81 ± 5	2.6	2018	38
Au/SC $MAPb_{0.985}Zn_{0.015}Br_3$/Au	1.6	25.5	6.33×10^8		2.67	2019	This work

Table 2 Comparison of photodetector properties of perovskite SCs

Single crystal	R_a [mA W^{-1}] @ V bias (light source, intensity)	D^* (Jones) @ V bias (light source, intensity)	Peak EQE/gain	Response time [ms]	Off/on	Year	Ref.
Au/Ti SC $MAPbCl_3$/Pt	46.9 @15 V (365 nm, 1 W cm^{-2})	1.2×10^{10} (365 nm 1 W cm^{-2})	—	24/62	1.1×10^3	2015	33
Au/SC $MAPbaI_3$/Au & Au/SC $MAPbaI_3$/C_{60}/Ga	35 to 0.19 @0.62–1.00 V (337 nm, 4 ns width)	—	12.6–15.8% (520–810 nm)	—	—	2015	34
Ti/SC $CsPbBr_3$/Ti & Au/SC $CsPbBr_3$/Au	28 (550 nm)	1.7×10^{11}	Over 6%	230/60	10^5	2017	34
Au/SC $MAPbBr_3$/Ga	—	2×10^{10}@ −4 (570 nm@ 6 μW cm^{-1})	3%@−4 V 570 nm	—	—	2015	39
Au/SC $MAPbBr_3$/Pt	2@ 0 V (white-light)	1.4×10^{10}@ 0 V (white-light)	—	0.07/0.15 (white-light)	—	2016	40
	100@ +3 V(white-light)	7.1×10^{11}@ +3 V (white light)					
	4.5 (350 nm)	3×10^{10}(350 nm)					
Au/SC $MAPb_{0.985}Zn_{0.015}Br_3$/Au	3.9 (532 nm)	2.36×10^{10} (532 nm at V_{ds} = 1 V)	—	23.3/24.2	—	2019	This work

Experimental section

Materials

Lead bromide (98%), zinc bromide (98%), methylammonium bromide (98%) and dimethylformamide (anhydrous, 99.8%) were purchased from Sigma Aldrich. All salts and solvents were used as received without any further purification.

Synthesis of $MAPbBr_3$ and $MAPbZnBr_3$ single crystals

A 1 : 1 molar solution containing $PbBr_2$ and MABr was prepared in DMF for $MAPbBr_3$, and a 0.9 : 0.1 : 1 molar solution containing $PbBr_2$, $ZnBr_2$ and MABr was prepared in DMF at room temperature, respectively. The solutions were filtered using a PTFE filter with 0.2 mm pore size. Two millilitres of the filtrate were placed in a vial and the vial was kept in an oil bath undisturbed at 80 °C. All procedures were carried out under ambient conditions and a humidity of 55–57%. The crystals used for measurements were grown for six months.

Structure characterization

The crystal structure of the Zn:$MAPbBr_3$ and $MAPbBr_3$ samples was characterized by X-ray powder diffraction (XRD) on a Bruker D8 Discover X-ray diffraction system. The metal contents of Zn and Pb were obtained by inductively coupled plasma optical emission spectroscopy (ICP-OES), and the weight content of Zn : Pb in the MPZB sample is 1.55 : 1000. Scanning transmission electron microscopy (STEM) and EDS mapping were performed a Talos FEI, which was equipped with four detectors. High resolution transmission electron microscopy (HRTEM) was performed using a cryo-TEM at liquid N_2 temperature.

UV-vis absorption and PL characterization

UV-vis absorption spectra were recorded at room temperature on a CRAIC Technologies UV-Visible-NIR microspectrophotometer. Steady-state PL spectra were measured using a Shamrock spectrometer (model no. SR-750-D1-R) and detected using a Newton CCD (model no. DU920P-BU). For the thermal stability test, the samples were placed in a vacuum chamber and excited with a 442 nm He–Cd laser (KIMMON IK5751I-G). The power of the excitation laser is 0.5 mW, and the spot size is ~0.007 cm^2. The temperature was controlled within a closed-cycle helium cryostat (CRYO Cool-G2B-LT) from 40 to 300 K. PL decay curves were obtained by using a time-correlated Hamamatsu H7422-02 photomultiplier tube.

Photodetector characterization

The size of 2.67 × 2.35 = 6.2745 mm^2 of the $MAPbZnBr_3$ single crystal was used to fabricate a photodetector by depositing ~50 nm thickness Au electrodes *via* the vacuum thermal evaporation method. The *I–V* characteristic of the device was measured using a Keithley4800 Source Meter, and the photocurrent was collected by illuminating the devices with 532 nm continuous laser @1 V. To illustrate the light-switching characteristic, the current under dark and illuminated conditions was controlled by a light shutter.

Conclusions

In conclusion, we have demonstrated the preparation and characterization of a non-toxic Zn doped $MAPbBr_3$ SC, which reveals superior optoelectronic properties and environmental stability. The main reason for the observation is that the introduction of Zn into $MAPbBr_3$ SC causes lattice strain (the atomic radius of the Zn is smaller than Pb), leading to the enhanced interaction between bonds. In addition, upon light illumination, the MPZB sample will undergo volumetric expansion in all directions to compensate the local lattice strain, resulting in improved structural stability even under long-term intensive light illumination. The Zn doping is also responsible for fewer defects of the SC, giving rise to less light quenching during the thermal stability measurement as well as better performance of the detector. This highly stable Zn doped $MAPbBr_3$ SC opens up a new possibility to engineer the properties of halide perovskite SCs, which might possess highly

stable optoelectronic properties and may prove beneficial for a number of applications.

Conflicts of interest

There are no conflicts to declare.

Acknowledgements

This work is supported by the Project funded by the China Postdoctoral Science Foundation (2019M661680), National Natural Science Foundation of China (11574130), Shenzhen Science and Technology Innovation Commission (Project No. KQJSCX20170726145748464, JCYJ20180305180553701, and KQTD2015071710313656), Leading Talents Program of Guangdong Province (2016LJ06N507) and Shenzhen Basic Research Fund (JCYJ20170817110652558), the Key Field R & D Program of Guangdong Province (2019B010941001), and National Key Research and Development Program of China, No. 2018YFB0704104.

References

1 Y. Liu, Z. Yang and S. Liu, *Adv. Sci.*, 2018, **5**, 1700471.
2 Y. Zhou, J. Chen, O. M. Bakr and H. T. Sun, *Chem. Mater.*, 2018, **30**, 6589–6613.
3 A. Swarnkar, W. J. Mir and A. Nag, *ACS Energy Lett.*, 2018, **3**, 286–289.
4 A. Kojima, K. Teshima, Y. Shirai and T. Miyasaka, *J. Am. Chem. Soc.*, 2009, **131**, 6050–6051.
5 M. Kim, G. H. Kim, T. K. Lee, I. W. Choi, H. W. Choi, Y. Jo, Y. J. Yoon, J. W. Kim, J. Lee, D. Huh, H. Lee, S. K. Kwak, J. Y. Kim and D. S. Kim, *Joule*, 2019, **3**, 2179.
6 E. H. Jung, N. J. Jeon, E. Y. Park, C. S. Moon, T. J. Shin, T. Y. Yang, J. H. Noh and J. Seo, *Nature*, 2019, **567**, 511–515.
7 Q. Dong, Y. Fang, Y. Shao, P. Mulligan, J. Qiu, L. Cao and J. Huang, *Science*, 2015, **347**, 967.
8 D. Shi, V. Adinolfi, R. Comin, M. Yuan, E. Alarousu, A. Buin, Y. Chen, S. Hoogland, A. Rothenberger, K. Katsiev, Y. Losovyj, X. Zhang, P. A. Dowben, O. F. Mohammed, E. H. Sargent and O. M. Bakr, *Science*, 2015, **347**, 519.
9 M. I. Saidaminov, A. L. Abdelhady, B. Murali, E. Alarousu, V. M. Burlakov, W. Peng, I. Dursun, L. Wang, Y. He, G. Maculan, A. Goriely, T. Wu, O. F. Mohammed and O. M. Bakr, *Nat. Commun.*, 2015, **6**, 7586.
10 Z. Liu, Y. Mi, X. Guan, Z. Su, X. Liu and T. Wu, *Adv. Opt. Mater.*, 2018, **6**, 1800413.
11 A. Zhizhchenko, S. Syubaev, A. Berestennikov, A. V. Yulin, A. Porfirev, A. Pushkarev, I. Shishkin, K. Golokhvast, A. A. Bogdanov, A. A. Zakhidov, A. A. Kuchmizhak, Y. S. Kivshar and S. V. Makarov, *ACS Nano*, 2019, **13**, 4140–4147.
12 A. Binek, F. C. Hanusch, P. Docampo and T. Bein, *J. Phys. Chem. Lett.*, 2015, **6**, 1249–1253.
13 X. Zheng, C. Wu, S. K. Jha, Z. Li, K. Zhu and S. Priya, *ACS Energy Lett.*, 2016, **1**, 1014–1020.
14 T. H. Han, J. W. Lee, C. Choi, S. Tan, C. Lee, Y. Zhao, Z. Dai, N. De Marco, S. J. Lee, S. H. Bae, Y. Yuan, H. M. Lee, Y. Huang and Y. Yang, *Nat. Commun.*, 2019, **10**, 520.
15 D. N. Dirin, L. Protesescu, D. Trummer, I. V. Kochetygov, S. Yakunin, F. Krumeich, N. P. Stadie and M. V. Kovalenko, *Nano Lett.*, 2016, **16**, 5866–5874.
16 R. Li, Z. Wei, H. Zhao, H. Yu, X. Fang, D. Fang, J. Li, T. He, R. Chen and X. Wang, *Nanoscale*, 2018, **10**, 22766–22774.
17 Q. Jiang, Y. Zhao, X. Zhang, X. Yang, Y. Chen, Z. Chu, Q. Ye, X. Li, Z. Yin and J. You, *Nat. Photonics*, 2019, **13**, 460–466.
18 Z. Wang, Z. Shi, T. Li, Y. Chen and W. Huang, *Angew. Chem., Int. Ed.*, 2017, **56**, 1190–1212.
19 Y. Liu, H. Lu, J. Niu, H. Zhang, S. Lou, C. Gao, Y. Zhan, X. Zhang, Q. Jin and L. Zheng, *AIP Adv.*, 2018, **8**, 095108.
20 Y. Zhou, Z. Zhou, M. Chen, Y. Zong, J. Huang, S. Pang and N. P. Padture, *J. Mater. Chem. A*, 2016, **4**, 17623–17635.
21 W. van der Stam, J. J. Geuchies, T. Altantzis, K. H. W. van den Bos, J. D. Meeldijk, S. Van Aert, S. Bals, D. Vanmaekelbergh and C. de Mello Donega, *J. Am. Chem. Soc.*, 2017, **139**, 4087–4097.
22 C. J. Bartel, C. Sutton, B. R. Goldsmith, R. Ouyang, C. B. Musgrave, L. M. Ghiringhelli and M. Scheffler, *Sci. Adv.*, 2019, **5**, eaav0693.
23 H. Tsai, R. Asadpour, J. C. Blancon, C. C. Stoumpos, O. Durand, J. W. Strzalka, B. Chen, R. Verduzco, P. M. Ajayan, S. Tretiak, J. Even, M. A. Alam, M. G. Kanatzidis, W. Nie and A. D. Mohite, *Science*, 2018, **360**, 67.
24 L. Wang, H. Zhou, J. Hu, B. Huang, M. Sun, B. Dong, G. Zheng, Y. Huang, Y. Chen, L. Li, Z. Xu, N. Li, Z. Liu, Q. Chen, L. D. Sun and C.-H. Yan, *Science*, 2019, **363**, 265.
25 R. Chen, Q. L. Ye, T. He, V. D. Ta, Y. Ying, Y. Y. Tay, T. Wu and H. Sun, *Nano Lett.*, 2013, **13**, 734–739.
26 Y. Fang, H. Wei, Q. Dong and J. Huang, *Nat. Commun.*, 2017, **8**, 14417.
27 N. Yi, S. Wang, Z. Duan, K. Wang, Q. Song and S. Xiao, *Adv. Mater.*, 2017, **29**, 1701636.
28 Q. Wang and W. Wu, *Opt. Lett.*, 2018, **43**, 4923–4926.
29 J. R. Ayres, *J. Appl. Phys.*, 1993, **74**, 1787–1792.
30 I. Capan, V. Borjanović and B. Pivac, *Sol. Energy Mater. Sol. Cells*, 2007, **91**, 931–937.
31 L. L. Kerr, S. S. Li, S. W. Johnston, T. J. Anderson, O. D. Crisalle, W. K. Kim, J. Abushama and R. N. Noufi, *Solid-State Electron.*, 2004, **48**, 1579–1586.
32 X. Chen, D. Wang, T. Wang, Z. Yang, X. Zou, P. Wang, W. Luo, Q. Li, L. Liao, W. Hu and Z. Wei, *ACS Appl. Mater. Interfaces*, 2019, **11**, 33188–33193.
33 G. Maculan, A. D. Sheikh, A. L. Abdelhady, M. I. Saidaminov, M. A. Haque, B. Murali, E. Alarousu, O. F. Mohammed, T. Wu and O. M. Bakr, *J. Phys. Chem. Lett.*, 2015, **6**, 3781–3786.
34 W. Nie, H. Tsai, R. Asadpour, J. C. Blancon, A. J. Neukirch, G. Gupta, J. J. Crochet, M. Chhowalla, S. Tretiak,

M. A. Alam, H. L. Wang and A. D. Mohite, *Science*, 2015, **347**, 522.

35 M. I. Saidaminov, M. A. Haque, J. Almutlaq, S. Sarmah, X.-H. Miao, R. Begum, A. A. Zhumekenov, I. Dursun, N. Cho, B. Murali, O. F. Mohammed, T. Wu and O. M. Bakr, *Adv. Opt. Mater.*, 2017, **5**, 1600704.

36 Z. Yang, Y. Deng, X. Zhang, S. Wang, H. Chen, S. Yang, J. Khurgin, N. X. Fang, X. Zhang and R. Ma, *Adv. Mater.*, 2018, **30**, 1704333.

37 H. Gao, J. Feng, Y. Pi, Z. Zhou, B. Zhang, Y. Wu, X. Wang, X. Jiang and L. Jiang, *Adv. Funct. Mater.*, 2018, **28**, 1804349.

38 Y. Liu, Y. Zhang, K. Zhao, Z. Yang, J. Feng, X. Zhang, K. Wang, L. Meng, H. Ye, M. Liu and S. Liu, *Adv. Mater.*, 2018, **30**, 1707314.

39 Y. Fang, Q. Dong, Y. Shao, Y. Yuan and J. Huang, *Nat. Photonics*, 2015, **9**, 679.

40 P. A. Shaikh, D. Shi, J. R. D. Retamal, A. D. Sheikh, M. A. Haque, C. F. Kang, J. H. He, O. M. Bakr and T. Wu, *J. Mater. Chem. C*, 2016, **4**, 8304–8312.